ACS APPLIED MATERIALS & INTERFACES

www.acsami.org

Research Article

Mechanistic Insights into the Superior DNA Delivery Efficiency of Multicomponent Lipid Nanoparticles: An In Vitro and In Vivo Study

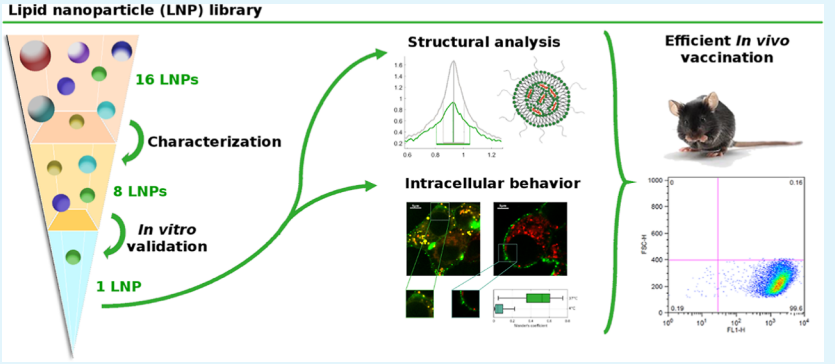
Erica Quagliarini, Junbiao Wang, Serena Renzi, Lishan Cui, Luca Digiacomo, Gianmarco Ferri, Luca Pesce, Valentina De Lorenzi, Giulia Matteoli, Heinz Amenitsch, Laura Masuelli, Roberto Bei, Daniela Pozzi, Augusto Amici, Francesco Cardarelli, Cristina Marchini,* and Giulio Caracciolo*

Cite This: *ACS Appl. Mater. Interfaces* 2022, 14, 56666−56677

Read Online

ACCESS | Metrics & More | Article Recommendations | Supporting Information

Downloaded via UNIV DEGLI STUDI DI TOR VERGATA on November 8, 2024 at 11:00:15 (UTC).
See https://pubs.acs.org/sharingguidelines for options on how to legitimately share published articles.



ABSTRACT: Lipid nanoparticles (LNPs) are currently having an increasing impact on nanomedicines as delivery agents, among others, of RNA molecules (e.g., short interfering RNA for the treatment of hereditary diseases or messenger RNA for the development of COVID-19 vaccines). Despite this, the delivery of plasmid DNA (pDNA) by LNPs in preclinical studies is still unsatisfactory, mainly due to the lack of systematic structural and functional studies on DNA-loaded LNPs. To tackle this issue, we developed, characterized, and tested a library of 16 multicomponent DNA-loaded LNPs which were prepared by microfluidics and differed in lipid composition, surface functionalization, and manufacturing factors. 8 out of 16 formulations exhibited proper size and zeta potential and passed to the validation step, that is, the simultaneous quantification of transfection efficiency and cell viability in human embryonic kidney cells (HEK-293). The most efficient formulation (LNP15) was then successfully validated both in vitro, in an immortalized adult keratinocyte cell line (HaCaT) and in an epidermoid cervical cancer cell line (CaSki), and in vivo as a nanocarrier to deliver a cancer vaccine against the benchmark target tyrosine-kinase receptor HER2 in C57BL/6 mice. Finally, by a combination of confocal microscopy, transmission electron microscopy and synchrotron small-angle X-ray scattering, we were able to show that the superior efficiency of LNP15 can be linked to its disordered nanostructure consisting of small-size unoriented layers of pDNA sandwiched between closely apposed lipid membranes that undergo massive destabilization upon interaction with cellular lipids. Our results provide new insights into the structure−activity relationship of pDNA-loaded LNPs and pave the way to the clinical translation of this gene delivery technology.

KEYWORDS: *lipid nanoparticles, gene delivery, transfection efficiency, membrane disintegration, vaccination*

INTRODUCTION

Considering the increasing impact of gene therapy and gene vaccines on the contemporary medical and epidemiological scenario, new strategies to tackle the limitations linked to the use of naked nucleic acids (NAs) in vivo are highly desirable. In this regard, it is well accepted that the employment of gene delivery systems (GDSs) increases the cellular uptake of NAs and protects them from nuclease-mediated degradation and phagocyte sequestration.[1,2] In the field, nonviral GDSs represent an attractive platform due to their higher safety profile. Among them, lipid-based nanoparticles (LNPs) proved to be chemically modifiable and poorly toxic or immunogenic GDS.[3] Most of the available LNPs are composed of a mixture of amino lipids generally comprising cationic or ionizable lipids (for 50%). Cationic lipids are naturally able to encapsulate NAs which are negatively charged.[4] Similarly, ionizable lipids are cationic at acid pH and neutral at physiological pH. This

Received: November 7, 2022
Accepted: December 6, 2022
Published: December 16, 2022



ACS Publications

© 2022 American Chemical Society

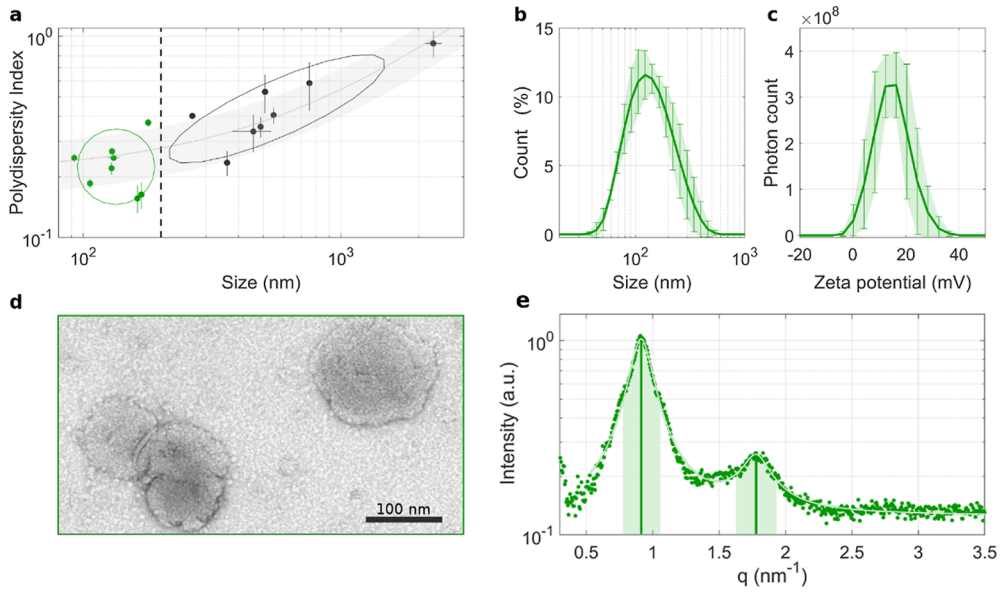


Figure 1. Synthetic identity of LNPs. (a) Scatter plot of PdI vs size for all the employed LNPs (green and black dots ± standard deviation). The vertical dashed line indicates the size threshold for further in vitro validations. The solid line indicates the best linear fit to the data. (b) Size distribution. (c) Zeta potential distribution. (d) Representative transmission electron microscopy (TEM) image for LNP15. (e) Synchrotron small-angle X-ray (SAXS) pattern of LNP15.

feature allows the interaction with the NA cargo during the synthesis procedure, performed using acid buffer, and later into the endosomal compartment promoting fusion with the cellular organelle membrane and leading to massive NA release into the cytosol.[5] The conventional methods to obtain lipid-based delivery systems (e.g., bulk mixing) are multistep procedures suffering from poor reproducibility and scalability. Innovations in manufacturing technology led to the shift to the most reproducible methods, including the microfluidic mixing.[6] This technique is based on the rapid mixing of two solutions, one constituted by the lipid dissolved in an organic solvent and another by NA in an aqueous buffer. These are forced to pass through thin channels in which lipids and NAs assemble under controlled conditions, generating small and monodisperse LNP suspension.[7] This single-step bottom-up approach ensures high reproducibility and lowers variability with respect to other synthesis procedures.[8] Furthermore, by changing manufacturing conditions such as lipid formulation, microfluidics parameters [total flow rate (TFR) and flow rate ratio], and the lipid/NA ratio, it is possible to tune the chemical−physical properties of LNPs, aiming to obtain safe and effective GDSs. Building on these technological improvements, lipid-based systems for siRNA and mRNA delivery are currently successfully employed in both pharmaceutics and vaccinology. For the first time in 2018, the FDA approved the clinical use of an LNP-formulated siRNA, ONPATTRO, which is used for the treatment of polyneuropathies caused by hereditary transthyretin-mediated amyloidosis.[9] The latest clinical success achieved by LNPs as a delivery system is the mRNA vaccines developed to face the SARS-Cov2 emergency (Moderna, BioNTech, and CureVac).[8] Despite the clinical successes obtained by lipid-based GDSs for mRNA and siRNA delivery, the same objective has not been achieved by LNPs encapsulating pDNA.

DNA vaccines are genetically engineered DNA plasmids that express an antigen. They reserve several advantages with respect to being RNA-based, including a lower cost of production, a higher thermostability (they do not require a strict cold chain for distribution), and an easier and more rapid manufacturing process. Thus, they represent a valuable alternative to mRNA vaccines. However, an efficient pDNA delivery system is still lacking. mRNA vaccines need to cross only one membrane to reach the cytoplasm, where they can be quickly translated into antigenic proteins, whereas DNA vaccines need to cross the cytoplasm and the nuclear membrane to be first transcribed in the nucleus and then translated in the cytoplasm. These differences make more difficult to develop LNPs for efficient DNA delivery with respect to RNA. To overcome this issue, physical methods of DNA delivery, such as electroporation, are usually used. They enhance cell transfection and consequently antigen expression and immune stimulation. Recently, two DNA vaccines developed against SARS-CoV-2, ZyCoV-D and INO-4800, demonstrated that DNA vaccines are safe and able to induce a protective immune response.[10−12] Vaccination with ZyCoV-D, administered intradermally via a needle-free injection system, was found to be efficacious and resulted in generation of both humoral and cellular response in a phase 3 clinical trial. INO-4800, when administered via intradermal injection followed by electroporation, displayed excellent safety, tolerability, and immunogenicity. However, widespread administration of DNA vaccines might be limited by the production of these physical devices (i.e., electroporators or injectors). Considering that the development of an effective DNA delivery system is essential to achieve therapeutic goals, in order to optimize LNP specifically conceived for pDNA delivery, in this work, we synthesized a library of multicomponent LNP formulations for DNA encapsulation which differed in lipid composition, surface functionalization, and manufacturing factors, and we explored their application in the delivery of an anticancer DNA vaccine. To assess the efficiency of the systems, we applied a multistep experimental strategy which starts from the intra-structural characterization of the LNPs to the in vitro and in vivo biological validation.

https://doi.org/10.1021/acsami.2c20019
ACS Appl. Mater. Interfaces 2022, 14, 56666−56677

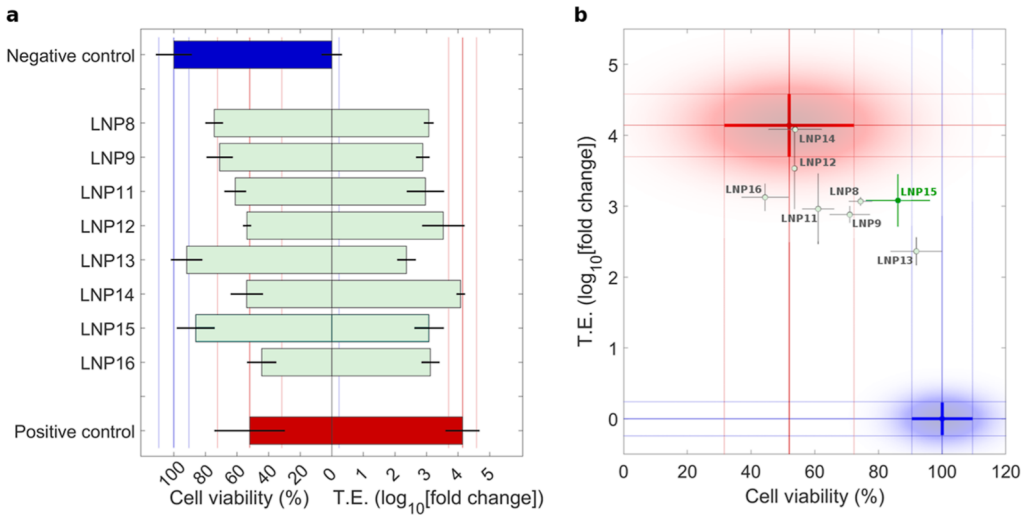


Figure 2. TE and cell viability of LNPs. (a) Histogram chart and (b) scatter plot of HEK-293 cell viability (with respect to nontreated cells) and TE (expressed as fold-change with respect to nontreated cells) for the LNP relationship.

We believe that our findings provide insights into the structure−activity relationship of DNA-loaded LNPs and contribute to filling the knowledge gap that still limits the clinical translation of this gene delivery technology.

RESULTS

Chemical−Physical Characterization of LNPs. A library of 16 LNPs with systematic changes in lipid composition was obtained through microfluidic mixing with plasmid DNA (pDNA) coding for the firefly luciferase reporter gene (Table S1 in the Supporting Information). LNPs were characterized for their size and zeta potential through dynamic light scattering (DLS) and microelectrophoretic measurements. The results are summarized in Table S2 in the Supporting Information. As shown in Figure 1a, the size of LNPs ranged from about 100 to 1000 nm, whereas the polydispersity index (PdI) values were found within the range between 0.1 and 0.5.

A positive correlation between size and PdI was detected, that is, the lower the particle size, the lower the PdI. This trend is depicted in Figure 1a as a solid line in a shaded area, which represents a linear correlation within the experimental errors. Thus, depending on the employed lipid mixture and mixing parameters, the microfluidic manufacturing procedure yielded monodisperse solutions of small LNPs (green dots) or less-homogeneous dispersions of large LNPs (black dots). According to the literature,[13] we set a threshold value of 200 nm as a cutoff size (indicated as a vertical dashed line in Figure 1a), beyond which LNPs were excluded from further analyses. Out of 16 formulations, 8 LNPs were smaller than the threshold, with an average size of about 130 nm and an average PdI of 0.235. Representative size distribution of a representative subthreshold LNP formulation (i.e., LNP15) is reported in Figure 1b, along with the corresponding zeta potential distribution (Figure 1c). Structural analysis was performed through TEM and synchrotron SAXS. TEM experiments (Figure 1d) confirmed the DLS findings, whereas synchrotron SAXS experiments were aimed at exploring the inner particle structure. A representative synchrotron SAXS pattern is shown in Figure 1e (green dots), along with the corresponding multi-Lorentzian fitting curve (solid line), according to eq 1. All the measured fitting parameters are listed in Table S3. The SAXS curve exhibited two broad Bragg peaks located at q_{100} = 0.91 nm^{-1} and q_{200} = 1.79 nm^{-1} (i.e., $q_{200} \approx 2q_{100}$), indicating a spatial periodicity along the normal direction to the lipid bilayer, with a d-spacing = $2\pi/q_{100}$ = 6.83 nm. This is the typical pattern of a lamellar lipid/DNA phase[14] whose repeating unit is made of a monolayer of hydrated DNA molecules (~2.5 nm) sandwiched between opposing lipid membranes ~4 nm thick. Interestingly, despite the amplitude decrease of the second peak with respect to the first one (i.e., $B < A$ in eq 1), no significant peak broadening was detected (i.e., $b \approx a$). The occurrence of Bragg peaks of equal width whose amplitudes decrease exponentially with the diffraction order is due to the thermal disorder of lamellar lattices.[15] This kind of disorder usually referred to as "first-order disorder" is generated by small fluctuations around well-defined positions of equal separation with the result that the structure factor decreases exponentially with the Debye−Waller temperature factor. Taking into account the full width at half-maximum (Δq = 0.22) of the Bragg peak, the average domain size of DNA−lipid layers can be measured by using the Debye−Sherrer relation: $Lm = 2\pi/\Delta q \sim 28$ nm. This value corresponds to an average domain size that is compatible with stacks made on average of N = 4 repeating units. SAXS experiments performed on the other LNP formulations provided similar results. The main difference was found for the average domain size, that is, in the number of repeating units. This aspect could play a key role in TE and shall be deeply discussed in the following sections.

In Vitro Validation: Transfection Efficiency and Cell Toxicity of LNPs. After completing the first step of the screening procedure, the eight selected LNPs were screened for their ability to induce firefly luciferase expression in a human embryonic kidney (HEK-293) cell line. Transfection reagent Lipofectamine 3000 was used as a positive control. As our goal was to achieve LNPs with high transfection efficiency (TE) and low toxicity, cell viability expressed as a percentage with respect to nontreated cells was assessed for each of the investigated systems. In Figure 2a, negative controls are reported as blue histograms having 100% cell viability and no luciferase expression (TE = 0), while positive controls are represented as red histograms and exhibited average TE = 4 and about 50% cell viability. Results for all the tested formulations are depicted as green histograms. The best

https://doi.org/10.1021/acsami.2c20019
ACS Appl. Mater. Interfaces 2022, 14, 56666−56677

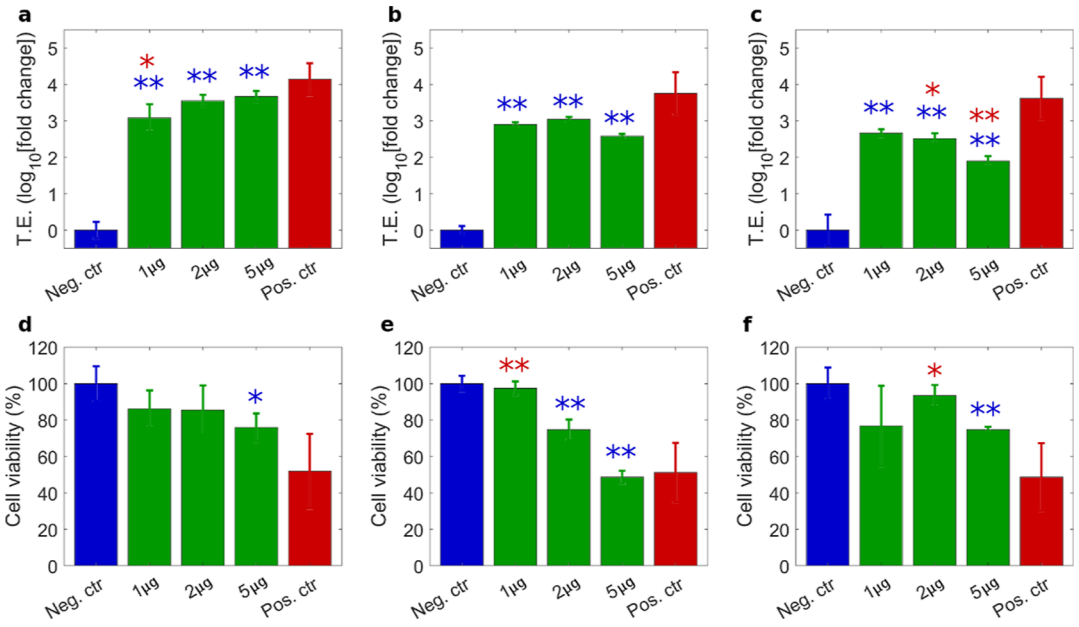


Figure 3. Effect of DNA dose on TE and cell viability of LNP15. TE and cell viability of LNP15 on (a,d) HEK-293, (b,e) HaCaT, and (c,f) CaSki cell lines at different pDNA amounts, as indicated in the *x*-tick labels. Statistical significance was evaluated by the *p*-value from Student's *t*-test; results with respect to negative and positive controls are expressed with blue and red *, respectively. $^{**}p < 0.01$, $^{*}p < 0.05$, no asterisks $p > 0.05$.

candidate among the LNPs included in the library can be identified by coupling TE and cell viability values in a scatter plot (Figure 2b). Each dot corresponds to a specific LNP, and its location is determined by the measured values of cell viability (*x*-axis) and TE (*y*-axis). Highly transfecting LNPs are generally cytotoxic, leading to cell viability values of about 50% (e.g., LNP12 and LNP14), whereas the most biocompatible system was the less performant as a transfecting agent (i.e., LNP13). LNP16, LNP8, and LNP15 exhibited comparable TE values but increasing cell viability, which read 40, 75, and 86%, respectively. Based on the results of Figure 2, LNP15 was identified as the most promising formulation for further validation as it exhibited the best compromise between high TE and good biocompatibility. Further considerations about the role of PEGylation and the lipid/DNA ratio on the TE of LNPs are reported in the Supporting Information.

Previous investigations[16] identified the DNA dose as a key factor regulating the transfection performances of lipid systems, thus we further validated LNP15 at three different doses (i.e., 1, 2, and 5 μg DNA/well) in HEK-293 cells. As the skin is a usual vaccination site due to its ability to induce both humoral and cellular immunity, we also transfected two epidermal cell lines, that is, immortalized adult keratinocytes (HaCaT) and epidermoid cervical cancer cells (CaSki) cells. TE and cell viability are shown in Figure 3a–f respectively. As Figure 3a–c clearly shows, the trend of TE as a function of the DNA dose was strictly dependent on the cell line. Administration of LNP15 to HEK-293 and CasKi resulted in TE boost and diminution, respectively. On the other hand, when HaCaT cells were treated with LNP15, TE showed poor dependence on the DNA dose. Cell viability decreased with the DNA dose in HEK-293 and HaCaT cells, while a minor effect was detected in CaSki cells.

As a final validation step of our study, we evaluated the ability of LNPs in delivering anti-HER2 DNA vaccine pVAX-hECTM both in vitro and in vivo. This cancer vaccine has been developed against the tyrosine-kinase receptor HER2, which is considered an ideal target in cancer immunotherapy due to its crucial role in the epithelial transformation and its selective overexpression in cancer tissues, such as breast cancer.[17−19] Since HER2 is exposed on the cell membrane, it can be targeted by both antibodies and cell-mediated immunity. It was previously reported that pVAX-hECTM is able to induce an antitumor immune response in breast cancer preclinical models when administered by electroporation.[20−22] Thus, we encapsulated the DNA vaccine into LNP15, while the less-effective formulation (i.e., LNP13) was used as a negative control. Immunofluorescence experiments reported in Figures 4 and in S1 in the Supporting Information were aimed at demonstrating that transiently transfected cells can express the oncoantigen HER2 encoded by the DNA vaccine and display it on the cell surface.

As shown in Figure 4a,b, HEK-293 cells were successfully transfected by LNP15 and, to a less extent, by LNP13. HER2 was exposed on the cell membrane, as required for inducing an effective humoral response. Then, the immunogenicity of pVAX-hECTM encapsulated in LNP15 or LNP13 was assessed by vaccinating C57BL/6 mice and evaluating the elicited anti-HER2 antibody response by FACS analysis. Of note, mice immunization with LNP15-pVAX-hECTM triggered a significantly higher antibody titer not only with respect to encapsulated empty plasmids (LNP15-pVAX, LNP13-pVAX) that were used as negative controls but also in comparison to LNP13-pVAX-hECTM that was not able to induce a detectable antibody production (Figure 4c,d).

Motivated by in vivo results, we explored the mechanisms of action of LNP15. An accepted paradigm in gene delivery states that efficient GDSs must be able to overcome transfection barriers and release the gene payload into the intracellular environment. Although the unbinding of DNA from lipid vesicles is not completely understood, several reports demonstrated that it depends on charge neutralization by cellular anionic lipids.[23] To estimate the role of this process, an established approach consists in mixing GDSs with negatively

https://doi.org/10.1021/acsami.2c20019
ACS Appl. Mater. Interfaces 2022, 14, 56666−56677

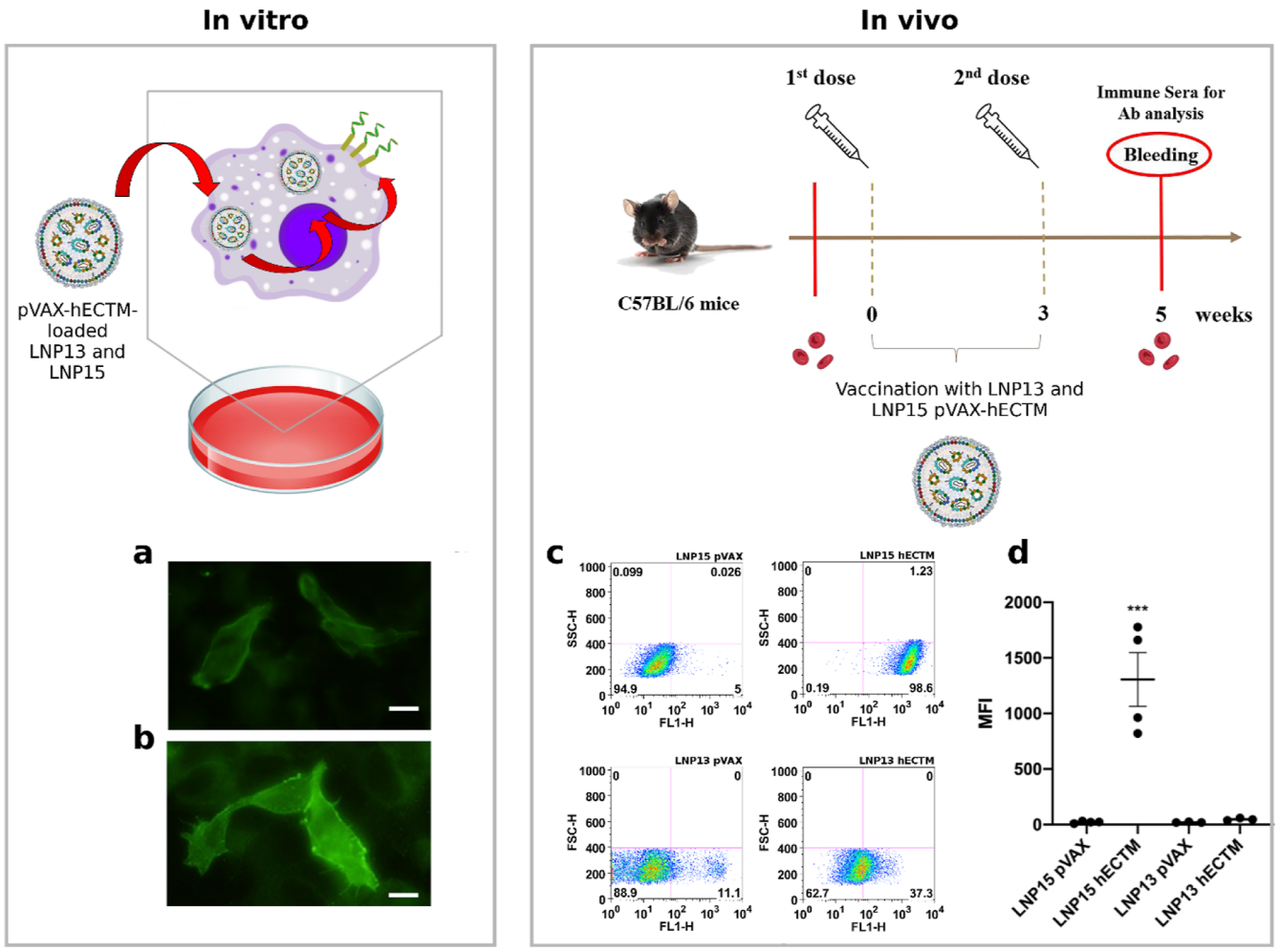


Figure 4. In vitro and in vivo validation of vaccine-loaded LNPs. HEK-293 cells were transiently transfected with the pVAX-hECTM-loaded LNP13 (a) and LNP15 (b) and analyzed under a fluorescence microscope 48 h after transfection. To detect the expression of the HER2 antigen in the membrane, trastuzumab was used as the primary antibody, and cells were stained using a secondary fluorescent antibody (Alexa-fluor 488). Magnification 40× (scale bar = 1 μm). (c) FACS analysis of the anti-HER2 antibody response induced in C57BL/6 mice (n = 4/experimental group) by the pVAX-hECTM vaccine in comparison with the pVAX1 empty vector (control), both encapsulated in LNP15 or LNP13, administered by intramuscular (i.m.) injections into the tibial muscle two times at 3 week intervals. Sera from immunized mice were harvested 2 weeks after the last booster and tested on SK-BR-3 target cells. (d) Mean fluorescence intensity (MFI). Data are shown as MFI ± SEM; t-test ****$P < 0.0001$.

charged anionic liposomes, intended as a model system of cellular membranes, and then measuring DNA release.[24] Indeed, this methodology proved to be a robust and versatile tool for predicting the TE of lipoplexes.[25] Thus, we incubated LNP15 with DOPG liposomes and quantified DNA release by fluorescence-based measurements. LNP13 was used as a negative control. As shown in Figure 5a, the amount of DNA released from LNPs monotonously increased as the DOPG/LNP mass ratio increased.

However, starting from the DOPG/LNP mass ratio = 0.5, LNP15 released significantly more DNA than LNP13. As a next step, we investigated the mechanism underlying such a different ability in releasing the gene payload. The research performed over the last two decades clarified that the structure of lipidic GDSs changes radically upon interaction with cellular lipids and that these changes are critical for endosomal escape.[25,26] It was also clarified that lipid mixing that leads to the fusion and formation of transient structures is the main factor controlling the release of the gene payload from lipid GDSs.[27] Thus, we employed synchrotron SAXS to verify whether the different abilities of LNP15 and LNP13 to release DNA may be related to their inner structure. As Figure 5b shows, the SAXS patterns of LNP15 and LNP13 exhibited a set of two equidistant Bragg peaks ($q_{001} \sim 0.9$ nm^{-1} and $q_{002} \sim 1.8$ nm^{-1}). On the other hand, the first-order Bragg peaks of LNP15 and LNP13 (Figure 5b, inset) had different heights and widths. In light of the above-reported considerations, we conclude that both formulations are made of locally ordered domains that are oriented in different directions. The main difference between the two structures resides in the spatial extension of the lamellar domains that is larger for LNP13 (compatible with $N > 6$ repeated units) than for LNP15 (compatible with $N = 4$ repeated units). Multilayered lipid systems have been long used in pharmacology to improve the structural stability against solubilization and fusion.[28] Moreover, it is also well known that the membrane stability of multilayered systems directly correlates with the number of layers. Therefore, we are tempted to conclude that the superior ability of LNP15 in releasing DNA may correlate with the low number of layers it is made of and, in turn, with a natural

https://doi.org/10.1021/acsami.2c20019
ACS Appl. Mater. Interfaces 2022, 14, 56666−56677

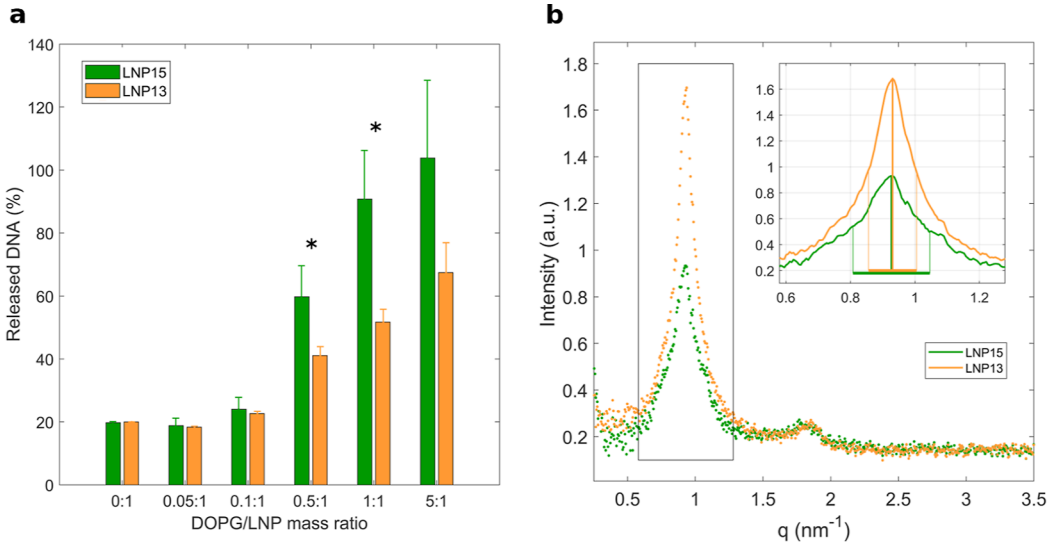


Figure 5. (a) Amount of pDNA released from LNP15 and LNP13 upon interaction with anionic liposome DOPG as a function of the DOPG/LNP mass ratio. (b) Synchrotron SAXS patterns of LNP15 and LNP13. The inset shows the first-order Bragg peaks.

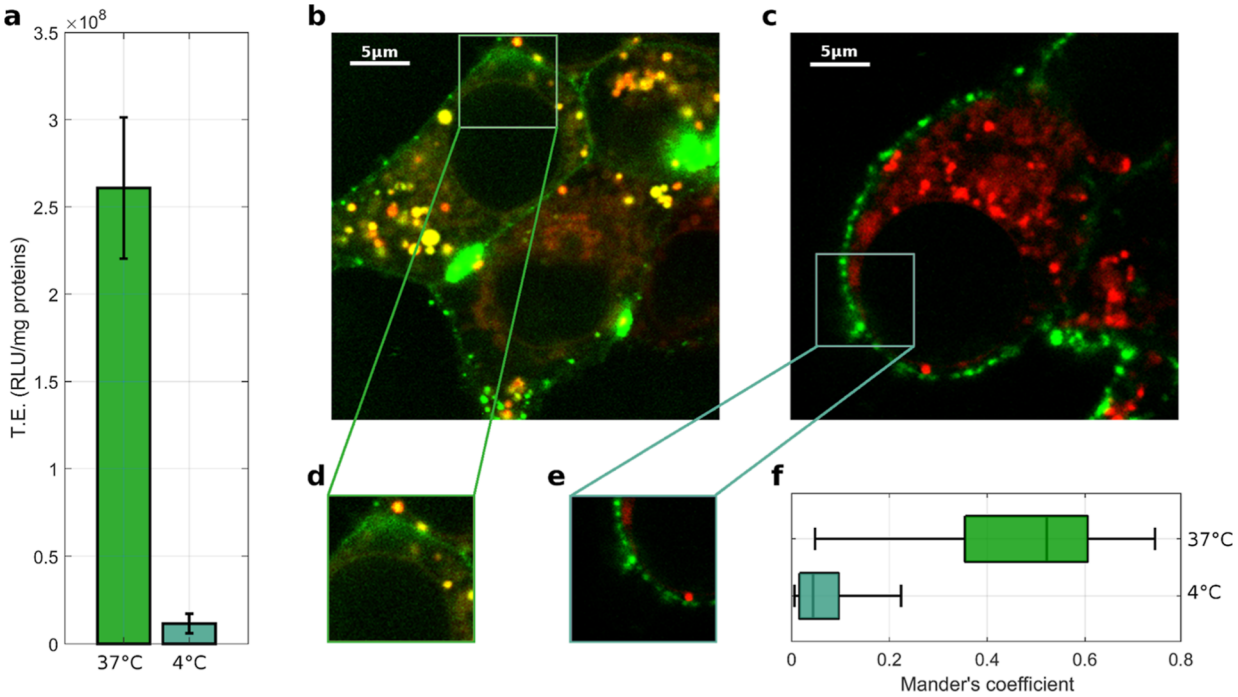


Figure 6. Mechanistic investigation of the intracellular behavior of LNP15. (a) TE of LNP15 at 37 and 4 °C. Confocal images of LNP15 (green channel) and lysosomes (red channel) after administration to HEK-293 cells at 37 (b) and 4 °C (c). Magnifications are displayed in (d,e). (f) Quantification of colocalization in terms of the green-to-red Mander's coefficient. Boxplots depict the distributions of measured values over datasets made of n = 10 images per class.

tendency to be destabilized by cellular membranes. In a series of previous investigations,[29,30] we used fluorescence confocal microscopy in live cells to explore the mechanisms of action of lipid systems at the cellular level. From previous investigations,[31] we learned that lipoplexes and nanoparticle systems enter the cells through a combination of energy-dependent (ED) and energy-independent (EI) mechanisms. ED internalization routes include some well-characterized endocytic pathways, such as phagocytosis, macropinocytosis, caveolar endocytosis, and clathrin-mediated endocytosis. On the other hand, EI internalization mechanisms include fusion, embedment, and direct translocation. These mechanisms are still poorly understood due to experimental limitations and are currently under investigation by computational methods.[32] It has been shown that EI processes may contribute to efficient cell internalization for some NP types. Thus, we first measure TE at 37 °C, where all the internalization mechanisms are active, and at 4 °C, where endocytosis is blocked and only EI uptake can take place. Results reported in Figure 6a show that at 4 °C, the TE of LNP15 is 1 order of magnitude lower than at 37 °C, suggesting a minor involvement of EI mechanisms in particle internalization. Among intracellular barriers to efficient gene delivery, lysosomal accumulation is probably the most rate-limiting one.[33] Upon entrapment within the lysosomal

https://doi.org/10.1021/acsami.2c20019
ACS Appl. Mater. Interfaces 2022, 14, 56666−56677

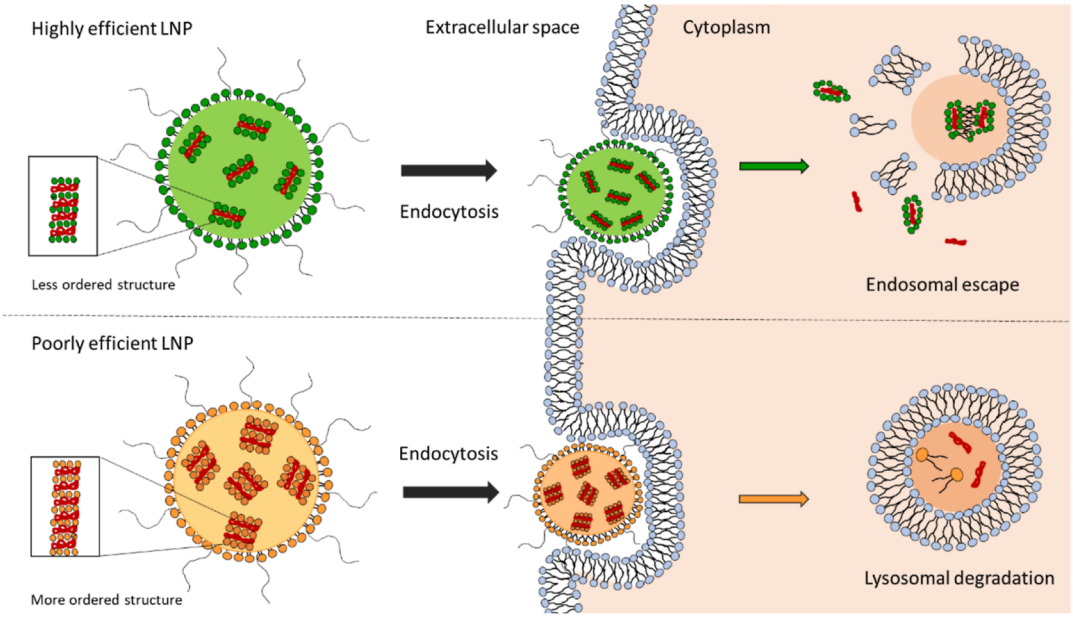


Figure 7. DNA-loaded LNPs exploit electrostatic attractions with the plasma membrane to drop off the repulsion barrier due to the "hydration force" between hydrated lipid bilayers. Particle cellular association is followed by endocytosis. Intracellular disintegration of the nanoparticle structure contributes to the discharge of DNA from highly efficient LNPs, thus creating optimized conditions for successful transfection.

compartment, LNPs undergo metabolic degradation and transfection fails. We, therefore, quantified the colocalization of LNP15 with lysosomes in HEK-293 cells at both 37 and 4 °C. Representative confocal images are reported in Figure 6b–e, where the green signal corresponds to fluorescently labeled lipids, the red signal identifies lysosomes, and two-channel colocalization is depicted as yellow pixels. At 37 °C, we observed that some intact fluorescently labeled LNPs colocalize with lysosomes (Figure 6b). The presence of these spot-like structures is compelling evidence of lysosomal accumulation. On the other hand, however, we noticed that large regions of the cell cytosol were uniformly stained in green (zoomed in Figure 6d). This peculiar fluorescence distribution does not originate from intact lipid vesicles and has been previously identified as a fingerprint of fusion-like mechanisms.[34] No diffuse fluorescence was observed when cells were treated with poorly efficient LNP13 (Figure S2 in the Supporting Information). In that case, the intracellular green fluorescence was only visible in the form of spot-like structures, presumably originating from intact vesicles. When experiments were replicated at 4 °C, such diffuse green fluorescence was not observed in cells but only localized at the cell membrane (Figure 6c and magnification in Figure 6e). Our TE and confocal microscopy results at 4 °C agree with recent findings showing that siRNA loaded LNPs bind to cell membranes at low temperature (0–4 °C) but are not effectively taken up by the cells with the result that their silencing activity is completely inhibited.[35] Indeed, LNP-lysosome colocalization was remarkably lower at 4 °C as compared to 37 °C, as calculated in Figure 6f by the Mander's coefficient that quantifies the portion of green pixels (the lipids) which colocalize with the red ones (the lysosomes).

Collectively, we conclude that robust intracellular disintegration by anionic cellular lipids can be the main factor accounting for the high TE of LNP15. This mechanism likely involves fusion with cellular membranes and is differentially activated depending on the lipid composition of the LNP formulation.

DISCUSSION

Most efforts have been devoted to encapsulating RNA in LNPs so far, while loading DNA has been only marginally investigated. Detailed knowledge of the structure and biological activity of pDNA-LNPs may extend the use of this emerging delivery technology to several biomedical applications that require the delivery of DNA instead of RNA. To fulfill this gap, this study started with a screening multistep procedure to optimize LNPs for DNA delivery and thus achieve highly efficient and not cytotoxic GDSs. As a first step, we designed a library of LNPs with systematic changes in influential factors (i.e., lipid composition, PEGylation, and microfluidic parameters) that are known to affect the physicochemical properties of GDSs.[36−38] To this end, 16 multicomponent LNPs were prepared through the microfluidic mixing of the lipid mixture dissolved in absolute ethanol and pDNA in acetate buffer. A threshold size was set to ∼200 nm according to the cutoff originally set by Torchilin and coworkers for GDSs in vivo.[13] The two- and three-component plain formulations were found to be larger in size than PEGylated LNPs. The increase in size correlated with the increase of their polydispersity and is likely due to the presence of aggregates and different-sized populations in the suspension. This finding confirms the relevance of PEGylated lipids, which are commonly used to avoid particle−particle interactions by creating a steric hindrance on the particle surface, as a critical ingredient of DNA-loaded LNPs.[39] We also observe that three out of four unPEGylated four-component LNPs had the proper size for in vitro validation. This result indicates that microfluidics determines the formation of LNPs whose size depends on the lipid species involved and their relative molar ratio. As most of the knowledge on the microfluidic LNP preparation is due to siRNA[40−42] or mRNA[43,44] encapsulating formulations while little is known of LNPs encapsulating

https://doi.org/10.1021/acsami.2c20019
ACS Appl. Mater. Interfaces 2022, 14, 56666−56677

pDNA,[45] we also explored the effect of the lipid/DNA weight ratio, R_w. LNP10, LNP11, and LNP12 were prepared for this purpose using the same lipid composition but encapsulating double and half the DNA dose (i.e., R_w = 5 and R_w = 20, respectively). This parameter had a great impact on the resulting LNPs as the size of the systems increased along with increasing DNA dose, while the zeta potential followed an opposite trend, that is, the much lower the DNA concentration, the more positive the particle charge. Finally, we changed the TFR from TFR = 2 to TFR = 8 mL/min in LNP15 and LNP16, respectively. Even with the same lipid composition and amount of encapsulated DNA, these LNPs were different in size and zeta potential as the increase in the flow rate caused an increase in size and PdI, along with an increase in positive charge. Globally, the physical−chemical characterization of the LNP library allowed us to demonstrate that PEGylation is fundamental to obtaining small-sized LNPs when the number of lipid components is less than 3. Increasing the number of lipid components ($n > 4$) is a valid strategy for keeping the size of the LNPs below a cutoff of 200 nm. Moreover, the lipid/DNA ratio and microfluidic parameters should be carefully evaluated. In our dataset, we found that high TE is usually accompanied by a reduction in cell viability as shown in Figure 3; both LNP12 and LNP14, even if as effective as the positive control (TE = 3.5 and 4, respectively), exerted nonnegligible toxicity on treated HEK-293 cells. With that in mind, we considered LNP15 the best compromise between high TE and biocompatibility, as this system was slightly less effective than the positive control, but considerably less toxic (85 vs. 50% cell viability). Furthermore, to find the best concentration for LNP15 in relation to the toxicity, three different concentrations were tested in three different cell lines, namely, HEK-293, HaCaT, and CasKi. The first cell line is a common cell line used for research purposes, while HaCaT and CasKi are epidermal cell lines that were selected given the potential use of LNPs for DNA vaccination. The TE of a lipofection system is dependent not only on the vector but also on the cell-to-cell differences. Depending on the cell type and their intracellular trafficking and uptake mechanism peculiarity, different cell lines may be easy- or hard-to-transfect.[46] The general trend observed for LNP15 indicated that increasing the particle dose administered to cells resulted in reduced cell viability, but this effect is not accompanied by a clear effect on TE. Finally, we studied LNP15-cell interaction at a cellular and subcellular level. The sketch reported in Figure 7 summarizes our mechanistic understanding of the LNP15−cell interaction. Electrostatic attractions let LNPs approach the anionic surface of the cell, and attachment is followed by endocytosis. Fluorescence confocal microscopy revealed that a portion of administered LNP15 underwent lysosomal degradation, while another one produced a diffuse intracellular fluorescence from labeled lipids (Figure 6). This is an unusual behavior for lipid systems (e.g., Lipofectamine 3000) as lipoplexes are usually observed as single spots in the cytosol.[47] On the other hand, the behavior of LNP15 resembles that of enveloped viruses that fuse with cellular membranes to infect cells.[48] With respect to viral particles, LNP15 exploits electrostatic attractions with the plasma membrane to lower the barrier due to the repulsive "hydration force" between hydrated lipid bilayers.[49] Combined TEM and synchrotron SAXS analyses show that LNP15 nanoparticles are small and made of unoriented layers of pDNA sandwiched between closely apposed lipid membranes. The reduced number of layers ($N = 4$) makes this formulation unstable against disintegration by cellular lipids. This event is likely to occur through interactions with anionic lipids that form ionic pairs with cationic lipids[50] and may induce the flattening and opening of LNPs. According to previous literature,[51] we suppose that the destabilization rate could depend upon the surface charge density and the lipid composition. This aspect deserves further consideration and will be addressed in future investigations. The instability observed for LNP15 is reminiscent of that reported for multicomponent lipoplexes which undergo entropy-driven mixing with cellular lipids leading to structure destabilization, endosomal escape, and massive DNA release in the cytoplasm.[52−55]

MATERIALS AND METHODS

Microfluidic Preparation of LNP−pDNA Complexes. Cationic lipids 1,2-dioleoyl-3-trimethyl-ammonium-propane and (3-[*N*-(N_0,N_0-dimethyl-aminoethane)-carbamoyl])-cholesterol, zwitterionic lipids dioleoyl phosphatidylethanolamine (DOPE), 1,2-dioleoyl-*sn*-glycerol-3-phosphocholine, cholesterol and PEG-lipids 1,2-dioleoyl-*sn*-glycerol-3-phosphoethanolamine-*N*-[amino(polyethylene glycol)-2000] and 1,2-distearoyl-*sn*-glycero-3-phosphoethanolamine-*N*-[amino(polyethylene glycol)-2000] were purchased from Avanti Polar Lipids (Alabaster, AL, USA). The plasmid used for LNP synthesis, pGL3 (firefly luciferase encoding plasmid), was purchased from Promega (Fitchburg, WI, USA). LNPs were obtained through a microfluidic mixing device (NanoAssemblr Benchtop from Precision NanoSystems Inc., Vancouver, BC, Canada) with a Y-shape staggered herringbone micromixer. All the formulations were prepared by dissolving lipids in different combinations and molar ratios in absolute ethanol to reach a final concentration of 12.5 mM. PmirGLO (Promega, Italy) was dissolved in 25 mM sodium acetate buffer (pH = 4), to 0.2 mg/mL. The organic solvent where lipids are dissolved and pDNA aqueous solutions are pumped by syringes into the microfluidic device, and at the Y-junction, they interact, forming LNP complexes. Two different TFRs (2 and 8 mL/min) were explored to get LNP complexes. The formulations were produced at different DNA/lipid weight ratios (R_w = 5, 10, and 20) corresponding to the nitrogen to phosphate charge ratio (N/P; nitrogen from the cationic lipid and phosphate from the NA) of 1.5, 3, and 6. After the micromixing process, the ethanol concentration decreases until 25% of the final LNP suspension volume. LNP complexes were subsequently loaded on dialysis cassettes (0.5−3 mL, MWCO 3 kDa, Thermo Scientific, Rockford, MI, USA) and dialyzed for 19 h against 500 mL of phosphate-buffered saline (PBS) at pH 7.4 to remove the residual ethanol.

Size and Zeta Potential Measurements. Particle size and zeta potential were measured by DLS and micro-electrophoresis at 25 °C using a Zetasizer Nano ZS90 (Malvern, UK). LNP suspensions were diluted 1:100 with distilled water for the measurements. Results are reported as mean ± standard deviation.

Transmission Electron Microscopy. TEM was performed using a TEM Morgagni 268D (Philips, the Netherlands). Briefly, samples (total volume = 8 μL) were dropped on formvar−carbon-coated copper grids (EMS, PA, USA) and allowed to adsorb for 5 min and then stained with a 2% uranyl acetate solution for 1 min at room temperature. Before the imaging, the excess staining solution was removed with filter paper.

Synchrotron Small-Angle X-ray Scattering. SAXS measurements were carried out at the Austrian SAXS station of the synchrotron light source ELETTRA (Trieste, Italy). A Pilatus3 1 M (Dectris, Baden, Switzerland) detector was employed for data acquisition and calibrated by using silver behenate powder (d-spacing = 58.376). The q-range was set within 0.05 and 5 nm^{-1}, with an exposure time of 10 s, which did not yield radiation damage. Correction for background, primary beam intensity, and detector efficiency were included in the analysis of SAXS patterns. SAXS

https://doi.org/10.1021/acsami.2c20019
ACS Appl. Mater. Interfaces 2022, 14, 56666−56677

patterns were finally fitted by a multi-Lorentzian function according to the following equation

$$I(q) = \sum_{i=1}^{M} \frac{A}{1 + i^2\left(\frac{q - q_a}{a}\right)^2} + \sum_{i=1}^{M} \frac{B}{1 + i^2\left(\frac{q - q_b}{b}\right)^2} + k \quad (1)$$

where the first and the second sum of Lorentzian functions describe the first and the second Bragg's peak, located at q_a and q_b, with the width proportional to a and b and amplitude equal to A and B, respectively. The fitting procedure converged for $M = 2$ with a goodness of $R^2 = 0.996$.

TE Assay. In vitro validation of the LNP library was achieved by transfection experiments on human embryonic kidney 293 (HEK-293) cells (ATCC, Rockville, MD, USA), human immortalized keratinocyte (HaCaT) cells, and the human cervical cancer (CaSki) cells (ATCC, Rockville, MD, USA). HEK-239 and HaCaT cell lines were grown in DMEM while the CaSki cell line in RPMI-1640 and supplemented with 10% FBS and maintained at 37 °C with 5% CO_2. In transfection experiments, cells were seeded on 24-well plates (40,000 cells per well). Each experiment has been performed in triplicates. Cells were treated with 1 μg formulated pDNA (PmirGLO expressing firefly luciferase, Promega, Italy). Three different DNA amounts 1, 2, and 5 μg per well were explored for LNP15. Lipofectamine 3000 was used as a positive control at 1 μg DNA per well following the standardized protocol (Life Technologies, Carlsbad, CA, USA). Cell lines were treated in an Opti-MEM medium (Life Technologies, Carlsbad, CA, USA), with selected LNPs (LNP8, LNP9, LNP11, LNP12, LNP13, LNP14, LNP15, LNP16) or Lipofectamine 3000 and then incubated for 3 h. After treatment, an appropriate medium supplemented by 20% FBS was added to each well to reach a final FBS concentration of 10%, and then cells were incubated at 37 °C. Luciferase expression was measured after 48 h through the luciferase assay system (Promega, Madison, WI, USA). Briefly, cells were washed in a phosphate saline buffer, and 60 μL of lysis buffer 1× (Promega) was added to each well. Then, 30 μL of the cell lysate was placed in three wells of white Corning 96Well Solid Polystyrene Microplate (Sigma-Aldrich, Milan, Italy). The 10 μL present in each well was diluted with 100 μL per well of the luciferase substrate (Promega), while the remaining 30 μL was divided into three wells (10 μL per well) and used for the BCA assay. The TE is expressed as relative light units per milligram of cell proteins, while the protein amount was determined by the Pierce BCA Assay Protein Kit (Thermo Fisher Scientific, Waltham, MA, USA). TE for the generic ith sample is expressed as the logarithmic fold change with respect to the TE of the negative control, that is,

$$\mathrm{TE}_i = \log_{10}\left(\frac{I_i/m_i}{I_0/m_0}\right) \quad (2)$$

where I_i and I_0 indicate the detected luminescence for the sample and the negative control, respectively, while m_i and m_0 represent the measured protein amount by the BCA assay for the sample and the negative control, respectively.

Cell Viability Assay. The cell viability of HEK-293, HaCaT, and CaSki cells was evaluated by 2,3-bis(2-methoxy-4-nitro-5-sulfophenyl)-2*H*-tetrazolium-5-carboxanilide (XTT assay, cell proliferation Kit II, Roche). Cells were seeded on 96-well plates (10,000 cells/well) for 24 h and incubated at 37 °C and 5% CO_2. Cells were treated with LNP complexes or Lipofectamine 3000 in an Opti-MEM medium for 3 h. After the treatment, DMEM 20% was added to HEK-293 and HaCaT cells and RPMI 20% to CaSki cells, and the cells were incubated for 48 h at 37 °C. Then, the XTT solution, prepared as indicated in the kit protocol, was added 50 μL per well, and cells were incubated at 37 °C for 3 h. After that, the absorbance (450−500 nm) was measured with the GloMax Discover System (Promega, Madison, WI, USA).

Confocal Microscopy. Live-cell imaging experiments were performed using a Zeiss LSM 800 confocal microscope equipped with a 63×, 1.4 N.A. oil immersion objective, and GaAsP detectors. Approximately 2×10^5 HEK-293 cells were seeded in a WillCo glass bottom dish (22 mm) 24 h before the experiment. On the day of confocal acquisitions, cells were incubated with LNP13- and LNP15-TexasRed 1× for 3 h at 37 °C (or 4 °C to inhibit endocytosis). About 30 min before confocal acquisition, cells were stained with LysoTracker DeepRed (Thermo Fisher) for lysosome staining. A series of confocal acquisitions (512 × 512 pixels, 50 nm pixel size) were conducted, and the cells stained with TexasRed were excited at 561 nm (HeNe laser), and the emission was collected in the 570−630 nm range. The cells stained with LysoTracker DeepRed were excited at 633 nm, and emission was collected in the 650−750 nm range. To evaluate the colocalization level between LNPs and lysosomes, Manders' and Pearson's correlation coefficients were calculated using the JaCoP plugin for ImageJ software.

Immunofluorescence. HEK-293 cells were plated in a 24-well plate (1×10^5 cells/well). One day after plating, 70−90% of confluent cells were transiently transfected with 1 μg pVAX-hECTM encapsulated in LNP15. 48 h after transfection, cells were fixed for 10 min with PBS-4% paraformaldehyde (Sigma, St. Louis, MO). After incubation in blocking buffer [PBS-10% bovine serum albumin (BSA; Sigma)] for 20 min, cells were incubated for 1 h at 37 °C with the primary antibody trastuzumab (anti-human HER2 antibody, 1:50). After washing, cells were incubated with Alexa Fluor 488-conjugated anti-human IgG secondary antibody (Invitrogen Molecular Probes, Eugene, OR) at a dilution of 1:200 for 1 h at 37 °C. Finally, cells were examined under a fluorescence microscope (Carl Zeiss GmbH, Germany) to assess the membrane expression of the oncoantigen HER2.

Vaccine Preparation. pVAX1 Vector (Life Technologies) and the DNA vaccine pVAX-hECTM (encoding the human extracellular and transmembrane domains of the human HER2 receptor; about 5000 bp) were transformed into *Escherichia coli* strain DH5-alpha and grown in Luria−Bertani medium supplemented with kanamycin. DNA plasmids were purified using a Maxiprep kit (Qiagen) for in vitro transfections and an EndoFree Plasmid-Giga kit (Qiagen, Chatsworth, CA, USA) for in vivo immunization, and their concentration was determined spectrophotometrically at 260 nm. pVAX1 and pVAX-hECTM were encapsulated in LNP15 and LNP13 nanoparticles by microfluidics.

Mice Experiments. C57BL/6 mice were housed under controlled temperature (20 °C) and circadian cycle (12 h light/12 h dark). The animals were fed on a chow diet (Mucedola) and tap water ad libitum. Mice were treated in accordance with the UK Animals (Scientific Procedures) Act, 1986, and associated guidelines, EU Directive 2010/63/EU for animal experiments, and with the 3Rs principles. All animal experiments were authorized by the Italian Ministry of Health (#708/2021-PR) and by the Animal Research Committee (OPBA) of the National Institute of Health and Science on Ageing (INRCA—Istituto Nazionale di Riposo e Cura per Anziani), Ancona (Italy). C57BL/6 male mice (8−10-week old) were immunized by i.m. injections into the tibial muscle two times at 3 week intervals with 100 μg of hECTM DNA vaccine or pVAX empty control vector encapsulated in LNP15 (4 mice/experimental groups). Two weeks after the last vaccination, blood was collected from the retro-orbital plexus under anesthesia. To collect serum, whole blood samples were left to clot at room temperature for 30 min. Serum separation was accomplished by centrifugation at 6000 rpm at 4 °C. Sera from immunized mice were analyzed by flow cytometry (BD FACSCalibur) using human HER-2 overexpressing SK-BR-3 cells as target cells. SK-BR-3 cells were obtained from American Type Culture Collection (Rockville, MD) and cultured in Dulbecco's modified Eagle's medium (DMEM, Gibco, Life Technologies) supplemented with 10% fetal bovine serum (FBS, Gibco, Life Technologies) and 1% penicillin−streptomycin (P/S) (Gibco, Life Technologies). Cells were maintained at 37 °C in an atmosphere of 5% CO_2. Briefly, subconfluent cells were detached and dispensed at a density of 10^6 cells per Falcon 5 mL round bottom polystyrene test tube. After a 3 min centrifugation at 1000 rpm at 4 °C, the obtained cell pellet was resuspended in staining buffer (0.05% NaN_3, 2% FBS in 1× PBS) and incubated with sera of vaccinated mice (1:40 dilution in staining buffer) for 1 h at 4 °C. After incubation, cells were washed three times

https://doi.org/10.1021/acsami.2c20019
ACS Appl. Mater. Interfaces 2022, 14, 56666−56677

and incubated with Alexa Fluor 488 goat anti-mouse IgG secondary antibody (1:200 dilution in staining buffer) for 1 h at 4 °C. Samples were washed three times with staining buffer and resuspended in 1× PBS, ready for analysis with BD FACSCalibur. Cell Quest Pro (version 6.0.2) and FlowJo (version 8.7) were used as acquisition and analysis software, respectively.

Statistical Information. The results of each experiment are reported as mean ± standard deviation of at least three replicates. Experimental errors are represented as error bars in scatter plots and histograms. Where indicated, the *p*-value from the two-tailed Student's *t*-test was computed to evaluate the statistical significance of the detected differences.

CONCLUSIONS

In this work, we investigated the structure−activity relationship of a library of 16 DNA-loaded LNPs with systematic changes in lipid composition and microfluidic mixing parameters. We individuated LNP15 as the most promising formulation by a step-by-step screening procedure ranging from physical−chemical characterization to in vitro validation and animal vaccination in vivo. This superior efficiency correlated with the particle nanostructure that was prone to be disintegrated by cellular lipids. This peculiar nanoscale arrangement induces DNA release and limits lysosomal degradation. Our results provide new insights into the correlation between the structure and functioning of DNA-loaded LNPs and pave the way to the clinical translation of this gene delivery technology.

ASSOCIATED CONTENT

Supporting Information

The Supporting Information is available free of charge at https://pubs.acs.org/doi/10.1021/acsami.2c20019.

Lipid composition and mixing parameters for the preparation of the LNPs; characterization of LNPs; fitting parameters of synchrotron SAXS data; in vitro validation of vaccine-loaded LNPs; and mechanistic investigation of the intracellular behavior of LNP13 (PDF)

AUTHOR INFORMATION

Corresponding Authors

Cristina Marchini − *School of Biosciences and Veterinary Medicine, University of Camerino, 62032 Camerino, Italy*; Email: cristina.marchini@unicam.it

Giulio Caracciolo − *NanoDelivery Lab, Department of Molecular Medicine, Sapienza University of Rome, 00161 Rome, Italy*; orcid.org/0000-0002-8636-4475; Email: giulio.caracciolo@uniroma1.it

Authors

Erica Quagliarini − *NanoDelivery Lab, Department of Molecular Medicine, Sapienza University of Rome, 00161 Rome, Italy*

Junbiao Wang − *School of Biosciences and Veterinary Medicine, University of Camerino, 62032 Camerino, Italy*

Serena Renzi − *NanoDelivery Lab, Department of Molecular Medicine, Sapienza University of Rome, 00161 Rome, Italy*

Lishan Cui − *School of Biosciences and Veterinary Medicine, University of Camerino, 62032 Camerino, Italy*; orcid.org/0000-0001-7647-1376

Luca Digiacomo − *NanoDelivery Lab, Department of Molecular Medicine, Sapienza University of Rome, 00161 Rome, Italy*

Gianmarco Ferri − *Laboratorio NEST, Scuola Normale Superiore, 56127 Pisa, Italy*

Luca Pesce − *Laboratorio NEST, Scuola Normale Superiore, 56127 Pisa, Italy*

Valentina De Lorenzi − *Laboratorio NEST, Scuola Normale Superiore, 56127 Pisa, Italy*; orcid.org/0000-0002-7429-6524

Giulia Matteoli − *Laboratorio NEST, Scuola Normale Superiore, 56127 Pisa, Italy*; orcid.org/0000-0003-2455-9557

Heinz Amenitsch − *Institute of Inorganic Chemistry, Graz University of Technology, 8010 Graz, Austria*

Laura Masuelli − *Department of Experimental Medicine, University of Rome "Sapienza", 00161 Rome, Italy*

Roberto Bei − *Department of Clinical Sciences and Translational Medicine, University of Rome "Tor Vergata", 00133 Rome, Italy*

Daniela Pozzi − *NanoDelivery Lab, Department of Molecular Medicine, Sapienza University of Rome, 00161 Rome, Italy*

Augusto Amici − *School of Biosciences and Veterinary Medicine, University of Camerino, 62032 Camerino, Italy*

Francesco Cardarelli − *Laboratorio NEST, Scuola Normale Superiore, 56127 Pisa, Italy*; orcid.org/0000-0003-3049-5940

Complete contact information is available at: https://pubs.acs.org/10.1021/acsami.2c20019

Author Contributions

E.Q. and J.W. contributed equally. Conceptualization was done by A.A., D.P., C.M., and G.C.; methodology was done by E.Q., J.W., S.R., L.C., G.F., L.P., V.D.L., G.M., H.A., L.M., R.B., D.P., F.C., A.A., C.M., and G.C.; investigation was done by E.Q., J.W., S.R., L.C., G.F., L.P., V.D.L., G.M., H.A., L.M., R.B.; writing of the original draft preparation was done by E.Q., S.R., L.D., D.P., F.C., and G.C.; writing with reviewing and editing was done by A.A., D.P., F.C., C.M., and G.C.; supervision was done by H.A., A.A., D.P., F.C., C.M., and G.C., and funding acquisition was done by F.C., D.P., and G.C. All authors have read and agreed to the published version of the manuscript.

Notes

The authors declare no competing financial interest.

ACKNOWLEDGMENTS

The research leading to the results reviewed here has received funding from the Sapienza University of Rome (grant no RM12117A87BA3B80 to G.C.) and from the Italian Minister for University and Research (MUR) for the research project "TITAN" (Nanotecnologie per l'immunoterapia dei tumori)—Programma PON ≪R&I≫ 2014−2020 (ARS01_00906 to G.C.). This work was supported in part by the European Research Council (ERC) under the Horizon 2020 Programme (grant agreement no 866127 to F.C., project "CAPTUR3D"). J.W. was supported by Fondazione Umberto Veronesi.

REFERENCES

(1) Harashima, H.; Hiraiwa, T.; Ochi, Y.; Kiwada, H. Size dependent liposome degradation in blood: in vivo/in vitro correlation by kinetic modeling. *J. Drug Targeting* **1995**, *3*, 253−261.

(2) Prabha, S.; Zhou, W.-Z.; Panyam, J.; Labhasetwar, V. Size-dependency of nanoparticle-mediated gene transfection: studies with fractionated nanoparticles. *Int. J. Pharm.* **2002**, *244*, 105−115.

(3) Fus-Kujawa, A.; Prus, P.; Bajdak-Rusinek, K.; Teper, P.; Gawron, K.; Kowalczuk, A.; Sieron, A. L. An Overview of Methods and Tools

for Transfection of Eukaryotic Cells in vitro. *Front. Bioeng. Biotechnol.* **2021**, *9*, 701031.
(4) Elouahabi, A.; Ruysschaert, J.-M. Formation and intracellular trafficking of lipoplexes and polyplexes. *Mol. Ther.* **2005**, *11*, 336−347.
(5) Semple, S. C.; Akinc, A.; Chen, J.; Sandhu, A. P.; Mui, B. L.; Cho, C. K.; Sah, D. W.; Stebbing, D.; Crosley, E. J.; Yaworski, E.; Hafez, I. M.; Dorkin, J. R.; Qin, J.; Lam, K.; Rajeev, K. G.; Wong, K. F.; Jeffs, L. B.; Nechev, L.; Eisenhardt, M. L.; Jayaraman, M.; Kazem, M.; Maier, M. A.; Srinivasulu, M.; Weinstein, M. J.; Chen, Q.; Alvarez, R.; Barros, S. A.; De, S.; Klimuk, S. K.; Borland, T.; Kosovrasti, V.; Cantley, W. L.; Tam, Y. K.; Manoharan, M.; Ciufolini, M. A.; Tracy, M. A.; de Fougerolles, A.; MacLachlan, I.; Cullis, P. R.; Madden, T. D.; Hope, M. J. Rational design of cationic lipids for siRNA delivery. *Nat. Biotechnol.* **2010**, *28*, 172−176.
(6) Zhigaltsev, I. V.; Belliveau, N.; Hafez, I.; Leung, A. K.; Huft, J.; Hansen, C.; Cullis, P. R. Bottom-up design and synthesis of limit size lipid nanoparticle systems with aqueous and triglyceride cores using millisecond microfluidic mixing. *Langmuir* **2012**, *28*, 3633−3640.
(7) Takagi, M.; Absalon, M. J.; McLure, K. G.; Kastan, M. B. Regulation of p53 translation and induction after DNA damage by ribosomal protein L26 and nucleolin. *Cell* **2005**, *123*, 49−63.
(8) Roces, C. B.; Lou, G.; Jain, N.; Abraham, S.; Thomas, A.; Halbert, G. W.; Perrie, Y. Manufacturing considerations for the development of lipid nanoparticles using microfluidics. *Pharmaceutics* **2020**, *12*, 1095.
(9) Garber, K. Alnylam launches era of RNAi drugs. *Nat. Biotechnol.* **2018**, *36*, 777−778.
(10) Kraynyak, K. A.; Blackwood, E.; Agnes, J.; Tebas, P.; Giffear, M.; Amante, D.; Reuschel, E. L.; Purwar, M.; Christensen-Quick, A.; Liu, N.; Andrade, V. M.; Diehl, M. C.; Wani, S.; Lupicka, M.; Sylvester, A.; Morrow, M. P.; Pezzoli, P.; McMullan, T.; Kulkarni, A. J.; Zaidi, F. I.; Frase, D.; Liaw, K.; Smith, T. R. F.; Ramos, S. J.; Ervin, J.; Adams, M.; Lee, J.; Dallas, M.; Shah Brown, A.; Shea, J. E.; Kim, J. J.; Weiner, D. B.; Broderick, K. E.; Humeau, L. M.; Boyer, J. D.; Mammen, M. P. SARS-CoV-2 DNA vaccine INO-4800 induces durable immune responses capable of being boosted in a phase 1 open-label trial. *J. Infect. Dis.* **2022**, *225*, 1923−1932.
(11) Mallapaty, S. India's DNA COVID vaccine is a world first−more are coming. *Nature* **2021**, *597*, 161−162.
(12) Khobragade, A.; Bhate, S.; Ramaiah, V.; Deshpande, S.; Giri, K.; Phophle, H.; Supe, P.; Godara, I.; Revanna, R.; Nagarkar, R.; Sanmukhani, J.; Dey, A.; Rajanathan, T. M. C.; Kansagra, K.; Koradia, P. Efficacy, safety, and immunogenicity of the DNA SARS-CoV-2 vaccine (ZyCoV-D): the interim efficacy results of a phase 3, randomised, double-blind, placebo-controlled study in India. *Lancet* **2022**, *399*, 1313−1321.
(13) Yuan, F.; Dellian, M.; Fukumura, D.; Leunig, M.; Berk, D. A.; Torchilin, V. P.; Jain, R. K. Vascular permeability in a human tumor xenograft: molecular size dependence and cutoff size. *Cancer Res.* **1995**, *55*, 3752−3756.
(14) Caracciolo, G.; Pozzi, D.; Caminiti, R.; Marchini, C.; Montani, M.; Amici, A.; Amenitsch, H. Enhanced transfection efficiency of multicomponent lipoplexes in the regime of optimal membrane charge density. *J. Phys. Chem. B* **2008**, *112*, 11298−11304.
(15) Pabst, G.; Koschuch, R.; Pozo-Navas, B.; Rappolt, M.; Lohner, K.; Laggner, P. Structural analysis of weakly ordered membrane stacks. *J. Appl. Crystallogr.* **2003**, *36*, 1378−1388.
(16) Palchetti, S.; Pozzi, D.; Marchini, C.; Amici, A.; Andreani, C.; Bartolacci, C.; Digiacomo, L.; Gambini, V.; Cardarelli, F.; Di Rienzo, C.; Peruzzi, G.; Amenitsch, H.; Palermo, R.; Screpanti, I.; Caracciolo, G. Manipulation of lipoplex concentration at the cell surface boosts transfection efficiency in hard-to-transfect cells. *Nanomed. Nanotechnol. Biol. Med.* **2017**, *13*, 681−691.
(17) Marchini, C.; Kalogris, C.; Garulli, C.; Pietrella, L.; Gabrielli, F.; Curcio, C.; Quaglino, E.; Cavallo, F.; Amici, A. Tailoring DNA vaccines: designing strategies against HER2-positive cancers. *Front. Oncol.* **2013**, *3*, 122.
(18) Pallerla, S.; Abdul, A. U. R. M.; Comeau, J.; Jois, S. Cancer vaccines, treatment of the future: With emphasis on her2-positive breast cancer. *Int. J. Mol. Sci.* **2021**, *22*, 779.
(19) Occhipinti, S.; Sponton, L.; Rolla, S.; Caorsi, C.; Novarino, A.; Donadio, M.; Bustreo, S.; Satolli, M. A.; Pecchioni, C.; Marchini, C.; Amici, A.; Cavallo, F.; Cappello, P.; Pierobon, D.; Novelli, F.; Giovarelli, M. Chimeric Rat/Human HER2 Efficiently Circumvents HER2 Tolerance in Cancer PatientsChimeric HER2 Vaccines Overcome Cancer Patient's T-cell Dysfunction. *Clin. Cancer Res.* **2014**, *20*, 2910−2921.
(20) Quaglino, E.; Mastini, C.; Amici, A.; Marchini, C.; Iezzi, M.; Lanzardo, S.; De Giovanni, C.; Montani, M.; Lollini, P.-L.; Masucci, G.; Forni, G.; Cavallo, F. A Better Immune Reaction to Erbb-2 Tumors Is Elicited in Mice by DNA Vaccines Encoding Rat/Human Chimeric ProteinsImmunogenicity of Chimeric Her-2/neu Vaccines. *Cancer Res.* **2010**, *70*, 2604−2612.
(21) Rolla, S.; Marchini, C.; Malinarich, S.; Quaglino, E.; Lanzardo, S.; Montani, M.; Iezzi, M.; Angeletti, M.; Ramadori, G.; Forni, G.; Cavallo, F.; Amici, A. Protective immunity against neu-positive carcinomas elicited by electroporation of plasmids encoding decreasing fragments of rat neu extracellular domain. *Hum. Gene Ther.* **2008**, *19*, 229−240.
(22) Jones, R. F.; Reyes, J. D.; Gibson, H. M.; Jacob, J. B.; Vaishampayan, U.; Ratner, S.; Chen, K.; Wei, W.-Z. An HER2 DNA vaccine with evolution-selected amino acid substitutions reveals a fundamental principle for cancer vaccine formulation in HER2 transgenic mice. *Cancer Immunol. Immunother.* **2019**, *68*, 1143−1155.
(23) Xu, Y.; Szoka, F. C. Mechanism of DNA Release from Cationic Liposome/DNA Complexes Used in Cell Transfection. *Biochemistry* **1996**, *35*, 5616−5623.
(24) Koynova, R.; Tarahovsky, Y. S.; Wang, L.; MacDonald, R. C. Lipoplex formulation of superior efficacy exhibits high surface activity and fusogenicity, and readily releases DNA. *Biochim. Biophys. Acta, Biomembr.* **2007**, *1768*, 375−386.
(25) Koynova, R.; Wang, L.; MacDonald, R. C. An intracellular lamellar−nonlamellar phase transition rationalizes the superior performance of some cationic lipid transfection agents. *Proc. Natl. Acad. Sci.* **2006**, *103*, 14373−14378.
(26) Caracciolo, G.; Marchini, C.; Pozzi, D.; Caminiti, R.; Amenitsch, H.; Montani, M.; Amici, A. Structural Stability against Disintegration by Anionic Lipids Rationalizes the Efficiency of Cationic Liposome/DNA Complexes. *Langmuir* **2007**, *23*, 4498−4508.
(27) Rehman, Z. u.; Hoekstra, D.; Zuhorn, I. S. Mechanism of Polyplex- and Lipoplex-Mediated Delivery of Nucleic Acids: Real-Time Visualization of Transient Membrane Destabilization without Endosomal Lysis. *ACS Nano* **2013**, *7*, 3767−3777.
(28) Gruner, S. M.; Lenk, R. P.; Janoff, A. S.; Ostro, N. J. Novel multilayered lipid vesicles: comparison of physical characteristics of multilamellar liposomes and stable plurilamellar vesicles. *Biochemistry* **1985**, *24*, 2833−2842.
(29) Cardarelli, F.; Pozzi, D.; Bifone, A.; Marchini, C.; Caracciolo, G. Cholesterol-Dependent Macropinocytosis and Endosomal Escape Control the Transfection Efficiency of Lipoplexes in CHO Living Cells. *Mol. Pharm.* **2012**, *9*, 334−340.
(30) Pozzi, D.; Marchini, C.; Cardarelli, F.; Amenitsch, H.; Garulli, C.; Bifone, A.; Caracciolo, G. Transfection efficiency boost of cholesterol-containing lipoplexes. *Biochim. Biophys. Acta, Biomembr.* **2012**, *1818*, 2335−2343.
(31) Marchini, C.; Pozzi, D.; Montani, M.; Alfonsi, C.; Amici, A.; Candeloro De Sanctis, S.; Digman, M.; Sanchez, S.; Gratton, E.; Amenitsch, H.; Fabbretti, A.; Gualerzi, C. O.; Caracciolo, G. Role of temperature-independent lipoplex−cell membrane interactions in the efficiency boost of multicomponent lipoplexes. *Cancer Gene Ther.* **2011**, *18*, 543−552.
(32) Lin, J.; Miao, L.; Zhong, G.; Lin, C.-H.; Dargazangy, R.; Alexander-Katz, A. Understanding the synergistic effect of physicochemical properties of nanoparticles and their cellular entry pathways. *Commun. Biol.* **2020**, *3*, 205.

(33) Cardarelli, F.; Digiacomo, L.; Marchini, C.; Amici, A.; Salomone, F.; Fiume, G.; Rossetta, A.; Gratton, E.; Pozzi, D.; Caracciolo, G. The intracellular trafficking mechanism of Lipofectamine-based transfection reagents and its implication for gene delivery. *Sci. Rep.* **2016**, *6*, 25879.
(34) Resina, S.; Prevot, P.; Thierry, A. R. Physico-chemical characteristics of lipoplexes influence cell uptake mechanisms and transfection efficacy. *PLoS One* **2009**, *4*, No. e6058.
(35) Nakamura, T.; Yamada, K.; Sato, Y.; Harashima, H. Lipid nanoparticles fuse with cell membranes of immune cells at low temperatures leading to the loss of transfection activity. *Int. J. Pharm.* **2020**, *587*, 119652.
(36) Caracciolo, G.; Pozzi, D.; Caminiti, R.; Marchini, C.; Montani, M.; Amici, A.; Amenitsch, H. Transfection efficiency boost by designer multicomponent lipoplexes. *Biochim. Biophys. Acta, Biomembr.* **2007**, *1768*, 2280−2292.
(37) Quagliarini, E.; Renzi, S.; Digiacomo, L.; Giulimondi, F.; Sartori, B.; Amenitsch, H.; Tassinari, V.; Masuelli, L.; Bei, R.; Cui, L.; Wang, J.; Amici, A.; Marchini, C.; Pozzi, D.; Caracciolo, G. Microfluidic Formulation of DNA-Loaded Multicomponent Lipid Nanoparticles for Gene Delivery. *Pharmaceutics* **2021**, *13*, 1292.
(38) Bigdeli, A.; Palchetti, S.; Pozzi, D.; Hormozi-Nezhad, M. R.; Baldelli Bombelli, F.; Caracciolo, G.; Mahmoudi, M. Exploring Cellular Interactions of Liposomes Using Protein Corona Fingerprints and Physicochemical Properties. *ACS Nano* **2016**, *10*, 3723−3737.
(39) Suk, J. S.; Xu, Q.; Kim, N.; Hanes, J.; Ensign, L. M. PEGylation as a strategy for improving nanoparticle-based drug and gene delivery. *Adv. Drug Delivery Rev.* **2016**, *99*, 28−51.
(40) Kulkarni, J. A.; Darjuan, M. M.; Mercer, J. E.; Chen, S.; van der Meel, R.; Thewalt, J. L.; Tam, Y. Y. C.; Cullis, P. R. On the formation and morphology of lipid nanoparticles containing ionizable cationic lipids and siRNA. *ACS Nano* **2018**, *12*, 4787−4795.
(41) Leung, A. K.; Hafez, I. M.; Baoukina, S.; Belliveau, N. M.; Zhigaltsev, I. V.; Afshinmanesh, E.; Tieleman, D. P.; Hansen, C. L.; Hope, M. J.; Cullis, P. R. Lipid nanoparticles containing siRNA synthesized by microfluidic mixing exhibit an electron-dense nanostructured core. *J. Phys. Chem. C* **2012**, *116*, 18440−18450.
(42) Walsh, C.; Ou, K.; Belliveau, N. M.; Leaver, T. J.; Wild, A. W.; Huft, J.; Lin, P. J.; Chen, S.; Leung, A. K.; Lee, J. B.; Hansen, C. L.; Taylor, R. J.; Ramsay, E. C.; Cullis, P. R.Microfluidic-based manufacture of siRNA-lipid nanoparticles for therapeutic applications. *Drug Delivery System*; Springer, 2014; pp 109−120.
(43) Shepherd, S. J.; Warzecha, C. C.; Yadavali, S.; El-Mayta, R.; Alameh, M.-G.; Wang, L.; Weissman, D.; Wilson, J. M.; Issadore, D.; Mitchell, M. J. Scalable mRNA and siRNA lipid nanoparticle production using a parallelized microfluidic device. *Nano Lett.* **2021**, *21*, 5671−5680.
(44) Lou, G.; Anderluzzi, G.; Schmidt, S. T.; Woods, S.; Gallorini, S.; Brazzoli, M.; Giusti, F.; Ferlenghi, I.; Johnson, R. N.; Roberts, C. W.; O'Hagan, D. T.; Baudner, B. C.; Perrie, Y. Delivery of self-amplifying mRNA vaccines by cationic lipid nanoparticles: The impact of cationic lipid selection. *J. Controlled Release* **2020**, *325*, 370−379.
(45) Ali, M. S.; Hooshmand, N.; El-Sayed, M.; Labouta, H. I. Microfluidics for Development of Lipid Nanoparticles: Paving the Way for Nucleic Acids to the Clinic. *ACS Appl. Bio Mater.* **2021**, DOI: 10.1021/acsabm.1c00732.
(46) Figueroa, E.; Bugga, P.; Asthana, V.; Chen, A. L.; Yan, J. S.; Evans, E. R.; Drezek, R. A. A mechanistic investigation exploring the differential transfection efficiencies between the easy-to-transfect SK-BR3 and difficult-to-transfect CT26 cell lines. *J. Nanobiotechnol.* **2017**, *15*, 36.
(47) Jaiprasart, P.; Yeung, B. Z.; Lu, Z.; Wientjes, M. G.; Cui, M.; Hsieh, C.-M.; Woo, S.; Au, J. L.-S. Quantitative contributions of processes by which polyanion drugs reduce intracellular bioavailability and transfection efficiency of cationic siRNA lipoplex. *J. Controlled Release* **2018**, *270*, 101−113.
(48) Harrison, S. C. Viral membrane fusion. *Virology* **2015**, *479*−*480*, 498−507.
(49) Parsegian, V. A.; Fuller, N.; Rand, R. P. Measured work of deformation and repulsion of lecithin bilayers. *Proc. Natl. Acad. Sci.* **1979**, *76*, 2750−2754.
(50) Pantazatos, D. P.; MacDonald, R. C. Directly Observed Membrane Fusion Between Oppositely Charged Phospholipid Bilayers. *J. Membr. Biol.* **1999**, *170*, 27−38.
(51) Pozzi, D.; Caracciolo, G.; Caminiti, R.; De Sanctis, S. C.; Amenitsch, H.; Marchini, C.; Montani, M.; Amici, A. Toward the rational design of lipid gene vectors: shape coupling between lipoplex and anionic cellular lipids controls the phase evolution of lipoplexes and the efficiency of DNA release. *ACS Appl. Mater. Interfaces* **2009**, *1*, 2237−2249.
(52) Marchini, C.; Pozzi, D.; Montani, M.; Alfonsi, C.; Amici, A.; De Sanctis, S. C.; Digman, M. A.; Sanchez, S.; Gratton, E.; Amenitsch, H.; Fabbretti, A.; Gualerzi, C. O.; Caracciolo, G. Role of temperature-independent lipoplex−cell membrane interactions in the efficiency boost of multicomponent lipoplexes. *Cancer Gene Ther.* **2011**, *18*, 543−552.
(53) Caracciolo, G.; Amenitsch, H. Cationic liposome/DNA complexes: from structure to interactions with cellular membranes. *Eur. Biophys. J.* **2012**, *41*, 815−829.
(54) Caracciolo, G.; Pozzi, D.; Amenitsch, H.; Caminiti, R. Multicomponent cationic lipid− DNA complex formation: Role of lipid mixing. *Langmuir* **2005**, *21*, 11582−11587.
(55) Muñoz-Úbeda, M.; Misra, S. K.; Barrán-Berdón, A. L.; Datta, S.; Aicart-Ramos, C.; Castro-Hartmann, P.; Kondaiah, P.; Junquera, E.; Bhattacharya, S.; Aicart, E. How does the spacer length of cationic gemini lipids influence the lipoplex formation with plasmid DNA? Physicochemical and biochemical characterizations and their relevance in gene therapy. *Biomacromolecules* **2012**, *13*, 3926−3937.

Recommended by ACS

Iterative Design of Ionizable Lipids for Intramuscular mRNA Delivery
Grayson Tilstra, Omar F. Khan, *et al.*
JANUARY 18, 2023
JOURNAL OF THE AMERICAN CHEMICAL SOCIETY
READ

On the Influence of Nucleic Acid Backbone Modifications on Lipid Nanoparticle Morphology
Kevin An, Jayesh A. Kulkarni, *et al.*
NOVEMBER 11, 2022
LANGMUIR
READ

Leveraging Biological Buffers for Efficient Messenger RNA Delivery via Lipid Nanoparticles
Michael I. Henderson, Gaurav Sahay, *et al.*
SEPTEMBER 21, 2022
MOLECULAR PHARMACEUTICS
READ

Interaction Kinetics of Individual mRNA-Containing Lipid Nanoparticles with an Endosomal Membrane Mimic: Dependence on pH, Protein Corona Formation, and Lipop...
Nima Aliakbarinodehi, Fredrik Höök, *et al.*
DECEMBER 13, 2022
ACS NANO
READ

Get More Suggestions >